





# Dispersion Analysis of Metasurfaces With Hexagonal Lattices With Higher Symmetries

SHIYI YANG <sup>1,2</sup> (Graduate Student Member, IEEE),  
OSKAR ZETTERSTROM <sup>2</sup> (Graduate Student Member, IEEE), FRANCISCO MESA <sup>3</sup> (Fellow, IEEE),  
AND OSCAR QUEVEDO-TERUEL <sup>2</sup> (Fellow, IEEE)  
(Regular Paper)

<sup>1</sup>School of Integrated Circuits and Electronics, Beijing Institute of Technology, Beijing 100081, China

<sup>2</sup>Division of Electromagnetic Engineering and Fusion Science, KTH Royal Institute of Technology, SE-100 44 Stockholm, Sweden

<sup>3</sup>Department of Applied Physics 1, ETS Ing. Informática, Universidad de Sevilla, 41012 Sevilla, Spain

CORRESPONDING AUTHOR: Oscar Quevedo-Teruel (e-mail: oscarqt@kth.se).

The work of Francisco Mesa was supported by the Grant PID2020-116739GB-I00 funded by MCIN/AEI/10.13039/501100011033. The work of Oscar Quevedo-Teruel was supported by the VR Project (2022-03865) through the Call Research Project within natural and engineering sciences.

**ABSTRACT** This article investigates the dispersion properties of metasurfaces with hexagonal lattices, including potential higher symmetric configurations. We explore the relationships between the periodicity of hexagonal lattices and their dispersion properties, paying special attention to how hexagonal periodic structures can be analyzed with either a hexagonal primitive unit cell or a rectangular supercell. We also study the possibility of introducing higher symmetries into hexagonal periodic structures, including glide symmetry and mirrored half-turn symmetry. To complement and validate the analysis, we designed a graded-index Luneburg lens antenna with a dielectric-filled hexagonal holey structure working in the  $K_a$ -band. The antenna generates steerable highly directive beams from 26 GHz to 30 GHz, which corroborates our analysis. Our findings provide valuable insight into the dispersion properties of hexagonal-lattice metasurfaces and demonstrate the feasibility of using such structures in practical applications.

**INDEX TERMS** Dispersion analysis, hexagonal lattice, irreducible Brillouin zone, glide symmetry, higher symmetries.

## I. INTRODUCTION

Metasurfaces are two-dimensional (2D) periodic structures commonly used in the design of microwave devices, such as waveguiding systems, filters, antennas, and lenses [1], [2], [3], [4]. The use of periodic elements makes it possible to manipulate wave propagation by locally modifying the geometric parameters of periodic inclusions, leading to rich properties for guided, scattered, and radiated waves [5]. Wave propagation features throughout the structure are typically described by dispersion diagrams. The dispersion diagram gives us the values of the components of the wavevector in terms of frequency, from which useful information can be derived such as phase velocity, group velocity, attenuation, and effective refractive index [6], [7], [8], [9], [10].

The modal fields in periodic media can be described with an infinite set of harmonics, termed space harmonics. All

space harmonics are represented in the dispersion diagram at periodic intervals from the fundamental harmonic. In other words, the phase constant of waves in a periodic structure is also periodic. The operation of the periodic structure can be completely characterized by its first repetition of the phase shift, known as the first Brillouin zone [6], [7]. In the microwave regime, great research effort has been devoted to studying the dispersion properties of 2D periodic structures, which are further applied to the designs of transmit/reflect arrays, frequency-selective surfaces, slow wave structures, etc [11], [12], [13], [14]. Although the fruitful qualitative dispersion properties provided by the introduction of higher symmetries in periodic structures were reported a few decades ago [15], [16], it has been in recent years that these higher symmetries have been exploited in microwave applications. In particular, twist and glide symmetries have been applied

to enhance the performance of waveguiding systems, lenses, leaky wave antennas, etc [17], [18], [19].

In most cases, periodic structures used in the microwave regime are tiled with square or rectangular unit cells. The analysis of such structures can be performed using commercial software or numerical methods [20], [21], [22], [23]. In recent years, more attention has been paid to periodic structures formed by non-rectangular unit cells because they provide additional design flexibilities and could potentially improve the performance of the periodic structures, among which hexagonal periodic structures have gained additional attention. Although the use of hexagonal periodic structures is common practice in material science [24], [25], [26], in lens design at microwave frequencies they have also shown their ability to reduce anisotropy and provide better performance compared to square metasurfaces [27]. In [28] a hexagonal periodic bandgap structure is combined with a microstrip antenna to expand its operating bandwidth. In [29], [30], [31], ultrawideband metamaterial absorbers are designed with hexagonal periodic structures to enable polarization sensitivity. Although the wave propagation characteristics are analyzed in these designs, limited attention is paid to the dispersion analysis of 2D hexagonal periodic structures. In [32], we present a hexagonal higher-symmetric dielectric periodic structure engineered to decrease the effective refractive index, thereby offering advantages for lens designs utilizing 3D printing technology. This research has extended the potential of hexagonal lattices in microwave component designs, emphasizing the necessities to gain a good understanding of the dispersion characteristic of these structures along with their enhanced symmetries.

In this article, and for the purpose of being illustrative, we perform a thorough analysis of 2D hexagonal periodic structures and illustrate the theoretical analysis with dispersion properties of a dielectric-filled holey hexagonal metasurface. The theoretical analysis starts by summarizing the underlying geometrical bases of the study of a periodic structure, as well as the relationships with its corresponding dispersion properties. Understanding these relationships has significant benefits, since it can advantageously guide the further design of practical devices. As is well known, the study of periodic structures is broken down into the analysis of a single unit cell, a task that is typically performed with the help of full-wave commercial software. However, this approach has limitations; for instance, hexagonal unit cells have more complex boundary conditions than square/rectangular unit cells, involving a larger number of boundaries and non-orthogonal adjacent boundaries. These complexities can pose challenges to the use of commercial simulators to deal with hexagonal metasurfaces and limit their use in practical applications. To overcome this drawback, here we propose a solution for obtaining the dispersion properties of a hexagonal unit cell by simulating a larger unit cell of rectangular shape, thereby providing a more familiar, flexible, and effective approach to analyzing periodic structures. We then study the impact of higher symmetries on hexagonal lattice metasurfaces to explore the compelling

potential characteristics that these higher symmetries can bring to the periodic structures. In addition to the glide symmetry studied in rectangular unit cells, a special symmetry called mirrored half-turn symmetry is investigated in the context of hexagonal lattice metasurfaces. The dispersion properties resulting from these higher symmetries are illustrated through simulation results of a specific hexagonal unit cell. To validate the previous theoretical analysis, a graded-index Luneburg lens antenna is designed, and its performance is analyzed with full-wave simulations. These simulations confirm the usefulness and validity of the theory.

The article is structured as follows. Section II-A provides an analysis of the geometrical periodicity of 2D periodic structures, while Section II-B describes its relationship with the periodicity of its dispersion property. Section II-C explains the methodology used to calculate the dispersion property of a hexagonal unit cell by simulating a larger rectangular supercell. Section III delves into some possible higher symmetries in hexagonal lattices, with glide symmetry discussed in Section III-A and mirrored half-turn symmetry in Section III-B. Section IV presents full-wave simulations of a Luneburg lens antenna designed on the basis of the previous theoretical study. Some relevant conclusions drawn from the study are finally presented in Section V.

## II. DISPERSION ANALYSIS OF A HEXAGONAL PERIODIC STRUCTURE

The design and properties of 2D hexagonal lattices have been discussed in depth in several previous works [7], [33]. This section provides a general overview of how to model them and calculate their dispersion diagrams, with a special emphasis on bringing our presentation closer to the language and tools commonly used in microwave/antenna engineering and focusing our study on the properties that are more relevant to the design of lens antennas.

The dispersion properties of a periodic structure are determined by its physical geometry and material characteristics. The periodicity of the physical structure in direct space (or real space) is defined using the so-called *direct* lattice, and the periodicity of the dispersion relations is defined in reciprocal space (or wavevector space) illustrated using the *reciprocal* lattice [6]. Importantly, the shape of the Brillouin zone can be derived from the reciprocal lattice. Next, we first analyze a hexagonal periodic structure in direct space and then discuss its dispersion properties in reciprocal space.

### A. DIRECT SPACE ANALYSIS

Our first hexagonal periodic structure under analysis is shown in Fig. 1. It consists of hexagonal holes filled with a dielectric material and carved mirror-symmetrically in the upper and lower plates of a parallel plate waveguide (PPW).

Any periodic structure can be seen as an infinite repetition of a certain element, denoted as a “unit cell”, and the unit cell of a periodic structure can be defined in many different

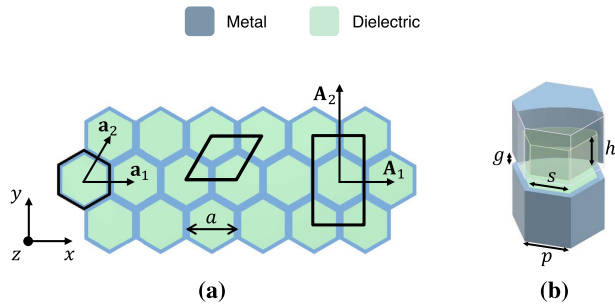


**FIGURE 1.** (a) 2D geometric configuration of a hexagonal holey periodic structure with holes placed mirror-symmetrically. Some possible unit cells are marked with solid black lines.  $a$  is the distance between the centers of two adjacent hexagonal unit cells. (b) 3D view of the unit cell with hexagonal shape.  $p$  is the side length of the unit cell,  $s$  is the side length of the dielectric filled hexagonal hole,  $h$  is the depth of the hole, and  $g$  is the height of the air gap.

ways, having different shapes and sizes [6], [7]. For example, Fig. 1(a) shows three possible unit cells, marked with solid black lines, of the 2D hexagonal periodic structure. The hexagonal and rhombic unit cells are the smallest-area unit cells that contain all the details of the periodic structure; that is, the *irreducible* unit cells. In comparison, the rectangular unit cell has a larger area and is called a *supercell*. Each unit cell of the periodic structure can be represented by a single point, regardless of their physical details, with this infinite array of points revealing the underlying geometry of the periodic structure. This array of points is called a *Bravais* lattice if its periodic arrangement is exactly the same from any of the points, including the number, distances, and relative positions of the neighboring points [6] (note that the vertices of the 2D honeycomb shown in Fig. 2(a) are not a Bravais lattice). When the Bravais lattice is defined in real space, it is known as the *direct* lattice. The direct lattice of a periodic structure can be different when different unit cells are chosen. Figs. 2(a) and (b) show the Bravais lattices of the structure under study when spanned by a hexagonal and rectangular unit cell, respectively.

To describe the arrangement of the Bravais 2D lattice, a pair of primitive vectors ( $\mathbf{a}_1$ ,  $\mathbf{a}_2$ ) is defined so that the array of points can be constructed as  $n_1\mathbf{a}_1 + n_2\mathbf{a}_2$ ,  $n_i \in \mathbb{Z}$ . In the case shown in Fig. 2(a), the primitive vectors are given by

$$\mathbf{a}_1 = a \hat{x}, \quad \mathbf{a}_2 = a \left( \frac{1}{2} \hat{x} + \frac{\sqrt{3}}{2} \hat{y} \right) \quad (1)$$

with  $a$  being the distance between the centers of the neighboring hexagonal unit cells. Similarly, the following pair of primitive vectors ( $\mathbf{A}_1$ ,  $\mathbf{A}_2$ ) is defined in Fig. 2(b):

$$\mathbf{A}_1 = a \hat{x}, \quad \mathbf{A}_2 = \sqrt{3}a \hat{y}. \quad (2)$$

It should be noted that the Bravais lattice only accounts for the underlying periodicity; that is, the Bravais lattice defined in real space does not contain information on the actual physical basis of the unit cell (also known as the “motif”). For example,

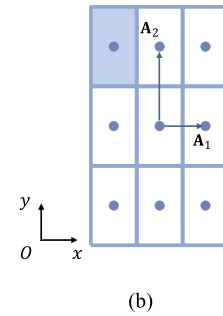
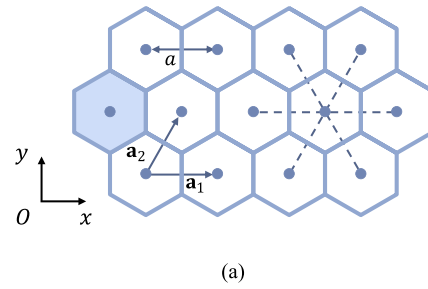


**FIGURE 2.** Bravais lattices in direct space when the hexagonal periodic structure is spanned with (a) the primitive unit cells and (b) the rectangular supercells. The Wigner-Seitz primitive cells are marked with solid blue lines in both lattices, with a WS cell highlighted in light blue in each lattice.

the motif of the holey periodic structure in Fig. 1 is the mirror-placed holes carved in the top and bottom metal plates.

To carry out a systematic analysis of the periodic structure, an area around a Bravais lattice point needs to be considered. This area is named the *primitive* cell when it meets two conditions: i) the area contains only one lattice point, and ii) the area tiles the entire space without overlapping by translations along the primitive vectors. A primitive cell of a Bravais lattice is then the smallest area that contains all the geometric information about the periodic structure. A particular primitive cell that describes the full symmetry of a Bravais lattice is the so-called Wigner-Seitz cell (WS cell) [6]. If the geometry of this cell is not very complicated, then this cell is the one usually chosen when studying the properties of a periodic structure. A WS cell can be constructed following three steps [6]: i) draw lines from a lattice point to all neighboring points [dashed lines in Fig. 2(a)]; ii) bisect the lines; iii) take the smallest polyhedron containing the point enclosed by these bisecting lines. In Fig. 2, WS cells are highlighted in light blue.

## B. RECIPROCAL LATTICE OF AN IRREDUCIBLE UNIT CELL

The connection between the Bravais lattices in direct and reciprocal space is discussed in this section. As the direct lattice varies with the choice of the unit cell, we first discuss the reciprocal lattice obtained when choosing an irreducible

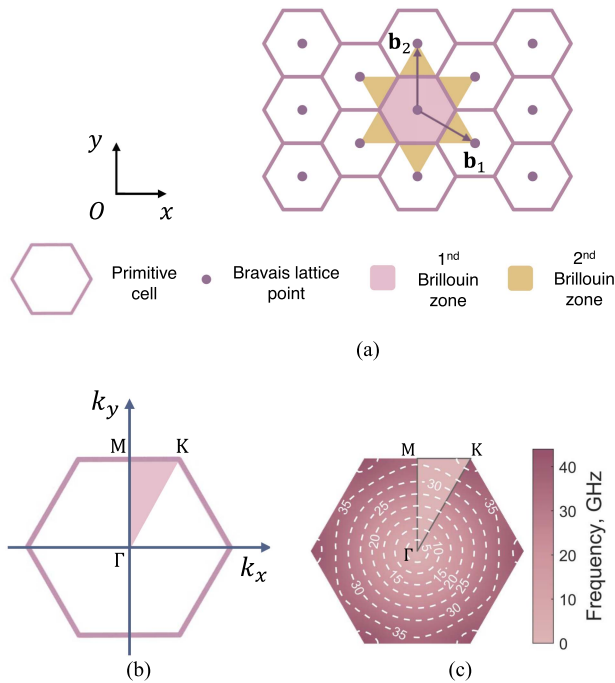


**FIGURE 3.** (a) Bravais lattice and WS primitive cells in the reciprocal space when an irreducible unit cell is selected in the direct space. The lattice is spanned by primitive vectors ( $\mathbf{b}_1$ ,  $\mathbf{b}_2$ ). The first and second Brillouin zones are colored pink and yellow, respectively. (b) Brillouin zone of the investigated hexagonal periodic structure spanned by irreducible unit cells. (c) Isofrequency map (2D dispersion diagram) of the fundamental mode in the periodic structure depicted in Fig. 1 with dimensions:  $p = 2$  mm,  $s = 1.7$  mm,  $h = 1.575$  mm,  $g = 0.6$  mm, and relative permittivity  $\epsilon_r = 2.33$ . The irreducible Brillouin zones with high-symmetry points  $\Gamma$ , M, and K are highlighted.

unit cell. Later, Section II-C discusses the case where a supercell is chosen and explores the relationship of the resulting reciprocal lattices when different unit cells are selected.

As explained in [6], [7], the reciprocal lattice contains information about the wavevectors of those plane waves (Bloch wavevectors) supported by the periodic structure. The intrinsic periodicity of these wavevectors (due to the  $2\pi$ -periodicity of the exponential function) also gives rise to a Bravais lattice, referred to as the *reciprocal* lattice. The primitive vectors that span the 2D reciprocal lattice can be derived from the primitive vectors of the direct lattice as follows:

$$\mathbf{b}_1 = \frac{2\pi}{S} \mathbf{a}_2 \times \hat{\mathbf{z}}, \quad \mathbf{b}_2 = \frac{2\pi}{S} \hat{\mathbf{z}} \times \mathbf{a}_1 \quad (3)$$

where  $S = |\mathbf{a}_1 \times \mathbf{a}_2|$  is the area of the unit cell in the direct space. In the case of our study, when the irreducible unit cell corresponding to the direct lattice shown in Fig. 2(a) is selected, the primitive vectors of the reciprocal lattice are given by

$$\mathbf{b}_1 = \frac{2\pi}{a} \left( \hat{\mathbf{x}} - \frac{1}{\sqrt{3}} \hat{\mathbf{y}} \right), \quad \mathbf{b}_2 = \frac{2\pi}{a} \frac{2}{\sqrt{3}} \hat{\mathbf{y}}. \quad (4)$$

The corresponding reciprocal lattice is illustrated by the pink points in Fig. 3(a). As is clearly expected, all the wavevector

information is included in any primitive cell of the reciprocal lattice.

However, the WS primitive cell is of particular interest, as it highlights the full symmetry of the wave propagation properties. This cell is known as the first Brillouin zone (BZ) and is marked pink in Fig. 3(a). To simplify the analysis as much as possible, the BZ can be further reduced by considering the combined symmetries of this cell with those of the motif, thus giving rise to the so-called irreducible BZ. Since the motif of the investigated hexagonal periodic structure also has hexagonal symmetry, the irreducible BZ is the shadowed triangular region in Fig. 3(b). Symmetry can be better visualized on the isofrequency map (a 2D dispersion diagram) presented in Fig. 3(c). This figure clearly shows that wavevector information in the full BZ can be completely reconstructed from that within the irreducible BZ. The analysis of the dispersion properties is usually simplified even more by only considering the wavevectors along the boundaries of the irreducible BZ; that is, obtaining a one-dimensional (1D) dispersion diagram only along the closed path  $\Gamma$ -M-K- $\Gamma$  in Fig. 3(c). Such results will be discussed in the following section.

### C. SUPERCELL RECIPROCAL LATTICE

When considering the rectangular supercell in Fig. 2, the reciprocal lattice of the investigated periodic structure is spanned by the following primitive vectors:

$$\mathbf{B}_1 = \frac{2\pi}{a} \hat{\mathbf{x}}, \quad \mathbf{B}_2 = \frac{2\pi}{a} \frac{1}{\sqrt{3}} \hat{\mathbf{y}}. \quad (5)$$

The corresponding reciprocal lattice is illustrated in Fig. 4(a) with pink points. A primitive WS cell (Brillouin zone) is also highlighted in pink in the figure. Its first BZ and isofrequency map are given in Figs. 4(b) and (c), with the irreducible BZ colored pink in both figures. It can be observed from Figs. 3(c) and 4(c) that, for the same periodic structure, the isofrequency map corresponding to the first BZ obtained with a supercell differs from that obtained from an irreducible unit cell. To understand their connections, we need to further investigate their corresponding direct and reciprocal lattices.

Brillouin zones that correspond to the irreducible unit cell, as well as the supercell, are marked with solid and dotted lines in Fig. 5(a). The supercell has a smaller first BZ, but its second BZ (obtained similarly to the first BZ, but instead considering the second neighbors) coincides with the first BZ of the irreducible unit cell, as indicated by the yellow areas in Figs. 4(a) and 5(a). In other words, the first BZ of a supercell lacks some of the Bloch wavevector information of the first BZ of the irreducible unit cell, a fact that is also apparent when comparing Figs. 3(c) and 4(c). This fact is akin to the aliasing phenomenon commonly found in the frequency-domain analysis of time signals [34]. To acquire the complete wavevector information provided by the hexagonal BZ when studying the rectangular supercell, we need to consider its first and second BZ's. A direct consequence of this fact is the appearance of additional modes when the dispersion diagrams are extended

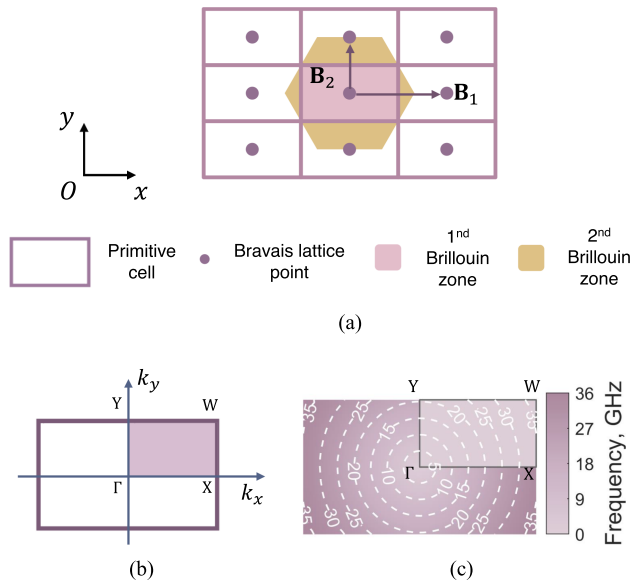


**FIGURE 4.** (a) Bravais lattice and WS primitive cells in the reciprocal space when the rectangular supercell is selected in the direct space. The lattice is spanned by primitive vectors ( $\mathbf{B}_1$ ,  $\mathbf{B}_2$ ). The first and second Brillouin zones are colored with pink and yellow, respectively. (b) Brillouin zone of the investigated periodic structure spanned by the selected rectangular supercell. (c) Isofrequency map of the fundamental mode. The irreducible Brillouin zones with high-symmetry points  $\Gamma$ ,  $Y$ ,  $W$ , and  $X$  are highlighted. The dimensions of the unit cell are given in Fig. 3.

to regions that belong to the second BZ. These additional modes are not spurious solutions; they provide redundant information that must be discerned.

The 1D dispersion diagram calculated with the HFSS eigenmode solver for propagation along the contour of the irreducible Brillouin zone shown in Fig. 3(c) for a primitive unit cell of the structure in Fig. 1 is shown in Fig. 5(b). The nontrivial application of this eigenmode solver to calculate the dispersion diagram is discussed in the Appendix A. Green dotted lines are the first two modes of the primitive unit cell, following the closed path  $\Gamma$ -M-K- $\Gamma$ . Curves with triangular markers [SC-1 in Fig. 5(b)] correspond to the first four modes supported by the rectangular supercell, following exactly the same path  $\Gamma$ -M-K- $\Gamma$ . As discussed above, part of the path is now in the second BZ of the rectangular supercell. Fig. 5(b) shows that two of the supercell modes perfectly match the two modes supported by the primitive unit cell. However, the other two modes are extra (redundant) modes that appear since the periodicities of the reciprocal lattices of the supercell and the primitive unit cell are different. Redundancy can be better understood if we observe in Fig. 5(a) that, in the supercell reciprocal space, the path  $\Gamma$ -M-K- $\Gamma$  is physically equivalent to the path  $M$ - $\Gamma$ -P- $M$  (translations of type  $m_1\mathbf{B}_1 + m_2\mathbf{B}_2$  correspond to the same physical situation). However, these two paths are clearly not equivalent when considered in the hexagonal Brillouin zone of the primitive unit cell. In fact, the two extra modes of the supercell can also be obtained by taking the path  $M$ - $\Gamma$ -P- $M$  when computing

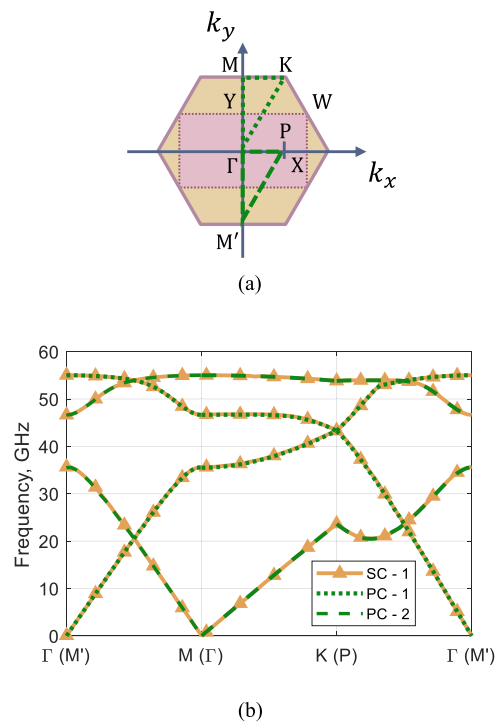


**FIGURE 5.** (a) Brillouin zones of the primitive unit cell (PC) and the rectangular supercell (SC). The hexagon represents the first Brillouin zone of the irreducible unit cell. The first and second Brillouin zones of the rectangular supercell are shaded with pink and yellow, respectively. Path  $\Gamma$ -M-K- $\Gamma$  (Path-1) and  $\Gamma$ -P-M'- $\Gamma$  (Path-2) are marked with dotted and dashed lines, respectively. (b) 1D dispersion diagrams. (SC-1:  $k$  along Path-1 calculated from SC. PC-1:  $k$  along Path-1 calculated from PC. PC-2:  $k$  along Path-2 calculated from PC.) The dimensions of the unit cell are given in Fig. 3.

the dispersion diagram of the primitive cell. These solutions correspond to the dashed green lines in Fig. 5(b), and more details of this calculation in the HFSS eigensolver are given in the Appendix A.

The above discussion makes it apparent that the dispersion diagram of a primitive cell can be retrieved from that of a supercell. The extra modes that appear in the supercell dispersion diagram can be identified by analyzing the equivalence of paths in the reciprocal space of both the primitive cell and the supercell. For instance, taking into account the reciprocal nature of the wave propagation in the structure, the path  $\Gamma$ -M' must give the same dispersion diagram as that of path  $\Gamma$ -M in the analysis of the primitive cell, and this is the reason why we find that the dashed modal curve corresponding to  $M$ - $\Gamma$  is a mirror version of the one corresponding to  $\Gamma$ -M. We can then conclude that this mathematical solution is the same physical solution as the one already obtained, although it could have been taken as another different mode of the supercell. This modal solution can be seen to be connected by continuity with other modal solutions that would correspond to having taken the path  $\Gamma$ -P-M' in the case of studying the primitive unit cell. It is then clear that all the dashed-line modal solutions of the supercell correspond to extra modes that will not appear in the study of the primitive cell. A similar rationale, based

on the identification of mirror-symmetry modal solutions in equivalent paths in the reciprocal space, can always be found for other choices of the supercell. This means that we can find a systematic way to discriminate the redundant extra modes found when applying the eigenmode solver of full-wave simulators to geometrically simpler supercells and still be able to retrieve the standard Brillouin diagram corresponding to the primitive unit cell.

Another interesting feature of the dispersion diagram of hexagonal periodic structures is the widely reported appearance of Dirac points [33], [35], [36], [37]. The peculiar properties of these points could have potential applications in microwave and millimeter wave components [38], [39], although this investigation is beyond the scope of this work.

### III. HIGHER SYMMETRIES IN HEXAGONAL PERIODIC STRUCTURES

In this section, we discuss the dispersion properties of the hexagonal periodic structure when two kinds of higher symmetries are introduced: glide symmetry and mirrored half-turn symmetry. Discussions are complemented by simulation results.

#### A. GLIDE SYMMETRIES IN THE HEXAGONAL LATTICE

A periodic structure has glide symmetry if it is invariant under translation and reflection [15], [16]. The electromagnetic properties of glide-symmetric periodic structures were initially studied around the 1970s [15], [16], [40], [41]. Recently, glide-symmetric structures have regained attention. Various benefits have been derived and applied to the design of microwave components [42], such as cost-effective gap-waveguide components [43], [44], filters [45], and lenses [18], [46], [47].

Hexagonal and rectangular periodic structures possess different periodicity characteristics that result in distinct glide-symmetric scenarios. Since previous studies have focused on rectangular cases, here we discuss glide symmetry in hexagonal periodic structures and their dispersion properties. The set of points that make up the Bravais direct lattice of a hexagonal periodic structure is illustrated in Fig. 6(a). The periodic structure can be tiled by translating a primitive unit cell into three directions:  $\mathbf{u}$ ,  $\mathbf{v}$ , and  $\mathbf{w}$ . The period  $p$  in any of these three directions is  $a$  [see Fig. 2(a)]. If the two layers of the structure studied (see Fig. 1) are off-shifted by  $p/2$  along two directions, a glide-symmetric configuration appears. A hexagonal periodic structure has three possibilities to synthesize glide symmetry depending on the translation vectors chosen, as illustrated in Fig. 6(b)–(d). In this figure, the two lattices associated with the top and bottom layers of the glide-symmetric periodic structure are presented in different blues, and a geometrical unit cell is shadowed in the middle. Taking the case in Fig. 6(b) as an example, the translation is carried out along the  $\mathbf{u}$  and  $\mathbf{v}$  directions, and the resulting structure is

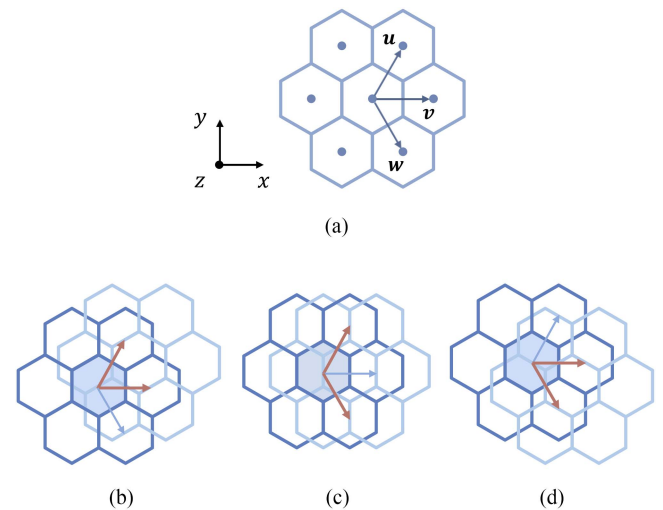


**FIGURE 6.** (a) The hexagonal lattice with translation directions. Possible glide symmetry configurations when translation along directions (b)  $\mathbf{u}$  and  $\mathbf{v}$ , (c)  $\mathbf{u}$  and  $\mathbf{w}$ , and (d)  $\mathbf{v}$  and  $\mathbf{w}$ . The corresponding translation directions are highlighted with brown arrows.

invariant after the following glide operation:

$$G_{\text{hex}}^{(w)} = \begin{cases} u & \rightarrow u + p/2 \\ v & \rightarrow v + p/2 \\ w & \rightarrow w \\ z & \rightarrow -z. \end{cases} \quad (6)$$

In this case, the double translation  $u-v$  is equivalent to having performed a unique translation of  $p/2$  along direction  $w$ . Consequently, this specific glide symmetry operator is denoted with superscript  $w$ . It can be observed that the lattices in Fig. 6(b)–(d) are related through a rotation of  $\pi/6$ ; that is, the three resulting lattices basically describe the same equivalent underlying periodic configuration.

The irreducible Brillouin zone is determined by the shape of the primitive cell and the pattern of the motif. As the dispersion diagram is constructed on the basis of the boundary of the irreducible Brillouin zone, it is essential to accurately define it. To demonstrate this, two examples are given: one with the motif having the same symmetry as the primitive cell outline (shown in Fig. 7) and another with the motif not having the same symmetry (shown in Fig. 8). If the motif has, at least, the same symmetries as the hexagonal outlined primitive cell [as happens for the dielectric-filled hexagonal hole shown in Fig. 7(a)], the geometrical unit cells resulting from its composition with the three glide-symmetric configurations in Fig. 6(b)–(d) are the same but rotated. It gives rise to a rotation of their corresponding dispersion properties that can be observed in the 2D isofrequency maps of the structures presented in Fig. 7(b)–(d).

However, if the motif does not possess the same symmetry as the cell outlined, the dispersion properties of the three glide configurations in Fig. 6(b)–(d) can be different. To break the symmetry of the hexagonal dielectric-filled hole cell presented in Fig. 7(a), the holes are taken rectangular and

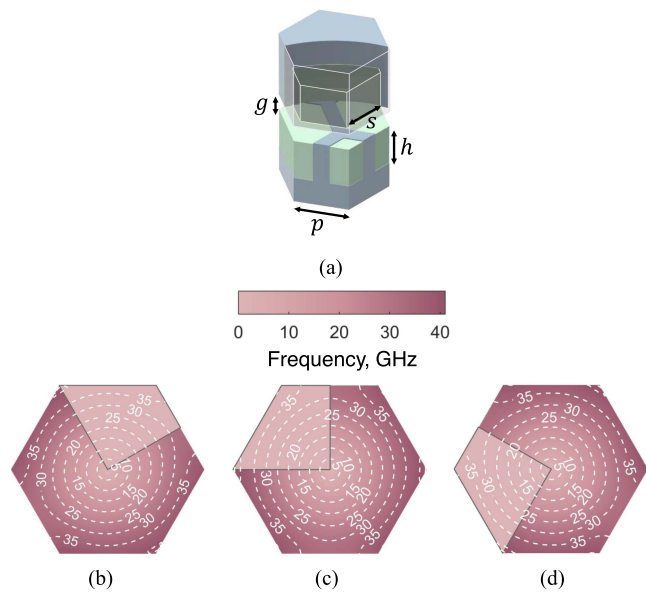


**FIGURE 7.** (a) 3D view of the glide-symmetric unit cell with dielectric-filled hexagonal holes. The dimensions of the unit cell are given in Fig. 3. Isofrequency maps of the fundamental mode for the glide-symmetric hexagonal periodic structure with irreducible Brillouin zone highlighted when (b) glide by  $u$  and  $v$ , (c) glide by  $u$  and  $w$ , (d) glide by  $v$  and  $w$ . Simulations are performed with the ANSYS HFSS eigenmode solver.

rotated  $20^\circ$  with respect to the  $x$ -axis, as shown in Fig. 8(a). The geometrical unit cells resulting from the three glide-symmetric conditions are shown in Fig. 8(a)–(c) when the same motif is used. It can be observed that the geometrical unit cells are different, which gives rise to an expected variation in their dispersion properties. The corresponding isofrequency maps are plotted in Fig. 8(d)–(f) together with the irreducible BZ, which now does not show any particular symmetry apart from reciprocity  $\omega(\mathbf{k}) = \omega(-\mathbf{k})$ .

## B. MIRRORED HALF-TURN SYMMETRY IN A HEXAGONAL LATTICE

Here, a particular case of higher symmetry in the hexagonal lattice is called mirrored half-turn symmetry. This higher symmetry can be defined by the following geometric operation:

$$\mathcal{H} = \begin{cases} \rho & \rightarrow & \rho \\ \phi & \rightarrow & \phi + \pi \\ z & \rightarrow & -z \end{cases} \quad (7)$$

expressed in the cylindrical coordinates shown in Fig. 9(a). The resulting structure has an arrangement as illustrated in Fig. 9(a), giving rise to the geometrical unit cell shown in Fig. 9(b). Note that the origin of the coordinate system can be placed in the center of any of the rhombic shapes created by the intersection of hexagonal outlines in the two layers. The isofrequency map of the simulated structure is shown in Fig. 9(c). Compared with the mirrored case in Fig. 3(c), which shows an isofrequency contour at 35 GHz almost circular within the first BZ, the 35 GHz isofrequency contour in Fig. 9(c) is already in the stopband region for the

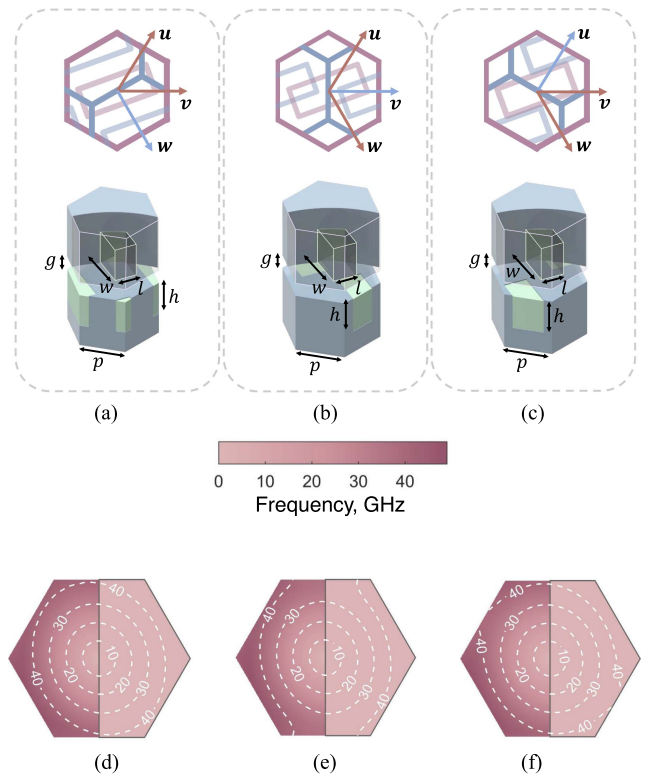


**FIGURE 8.** (a)–(c): Top and 3D views of the simulated glide-symmetric hexagonal structure with rotated dielectric-filled rectangular holes when (a) glide by  $u$  and  $v$ , (b) glide by  $u$  and  $w$ , (c) glide by  $v$  and  $w$ . The outlines of the unit cells and inclusions are marked with blue and pink in the top views (indicating the different layers), with translation directions highlighted with brown arrows. The holes are rotated  $20^\circ$  with respect to the  $v$  axis.  $p$  is the side length of the unit cell,  $w$  and  $l$  are the side lengths of the rectangular holes,  $h$  is the depth of the holes, and  $g$  is the height of the air gap. (d)–(f): Isofrequency maps of the fundamental mode for the glide-symmetric hexagonal periodic structure with rotated rectangular holes when (d) glide by  $u$  and  $v$ , (e) glide by  $u$  and  $w$ , (f) glide by  $v$  and  $w$ . Irreducible Brillouin zones are highlighted. The dimensions of the unit cells are:  $p = 2$  mm,  $h = 1.575$  mm,  $w = 2.5$  mm,  $l = 1$  mm, and  $g = 0.6$  mm.

case of mirrored half-turn symmetry in some directions. This implies that the mirrored half-turn symmetric structure has an overall higher refractive index while maintaining good isotropy, which could be beneficial in some applications, such as graded-index lens designs.

## IV. FULL-WAVE VALIDATION

Microwave lenses play a crucial role in various applications, including beamforming and antenna design, such as the Luneburg lens [48], [49] and Rotman lens [50], [51]. Metasurfaces offer significant benefits in lens design, as they enable precise control over microwave propagation directions by tuning the inclusions of the unit cell locally. In this article, we validated the theory by presenting the results of the full-wave simulation results of a  $K_a$ -band Luneburg lens antenna. In this work, only simulation results are provided, but simulations of similar antenna designs are widely reported in excellent agreement with the experimental results [4], [52]. A Luneburg lens is a rotationally symmetric graded-index lens

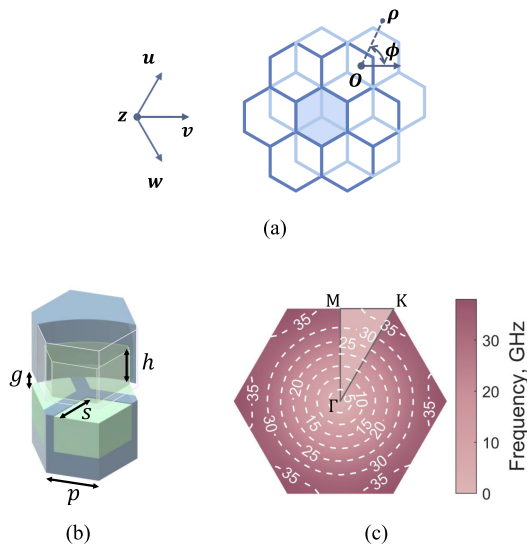


**FIGURE 9.** (a) mirrored half-turn symmetry configuration of the hexagonal lattice with translation directions. (b) Simulated dielectric-filled holey hexagonal unit cell of the structure under study. (c) Isofrequency map for the fundamental mode of the simulated structure. Simulations are performed in the ANSYS HFSS eigenmode solver. An irreducible Brillouin zone with high-symmetry points  $\Gamma$ , M, and K highlighted. The values of the geometric parameters and the dielectric permittivity of the unit cell are the same as those in Fig. 1.

that, when fed from its contour, produces a direct beam in the diametrically opposite direction. The refractive index profile of a Luneburg lens is given by

$$n(\rho) = \sqrt{2 - \left(\frac{\rho}{R}\right)^2} \quad (8)$$

where  $\rho$  is the radial position in the lens and  $R$  is the radius of the lens. The refractive index is 1 at the contour of the lens, thus avoiding reflection in the transition between the lens and the surrounding space. Due to its rotational symmetry, a Luneburg lens antenna can realize beam steering by feeding from different positions along the contour. In our design, the Luneburg lens is implemented in a PPW configuration. The required refractive-index distribution is realized by quasi-periodically loading the two PPW conductors with dielectric-filled hexagonal holes arranged according to the mirror half-turn symmetry. The unit cell has the same configuration as that of Fig. 9(b), with a substrate having  $\epsilon_r = 2.7$ .

This unit cell configuration is chosen for two reasons: 1) it offers a higher effective refractive index compared to the conventional unit cell with the same design parameters, as shown in Fig. 10, and 2) it provides better isotropy than glide symmetric unit cells, as evident when comparing the iso-frequency maps in Fig. 7 and Fig. 9. Fig. 11 shows the effective refractive indices as a function of frequency for different values of the hole size  $s$ . By tuning the hole size of each unit cell, we can replicate the effective refractive index distribution of a Luneburg lens. This procedure has been broadly used in the literature [42], although for completeness, the design steps have been summarized in the Appendix B.

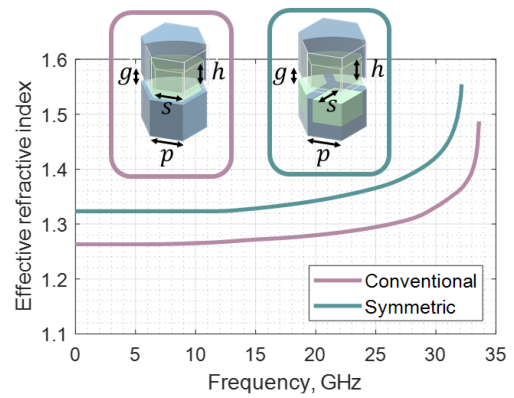


**FIGURE 10.** Effective refractive index versus frequency for the conventional (purple) and mirrored half-turn symmetric (green) structures. Structural parameters:  $p = 2$  mm,  $h = 1.575$  mm,  $g = 0.6$  mm,  $s = 1.85$  mm, and relative permittivity of the substrate  $\epsilon_r = 2.7$ .

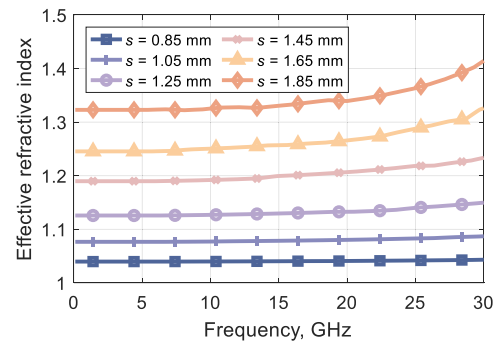


**FIGURE 11.** Effective refractive index versus frequency for a hexagonal periodic structure with a unit cell as in Fig. 9(b) with  $p = 2$  mm,  $h = 1.575$  mm,  $g = 0.6$  mm, and  $\epsilon_r = 2.7$ .

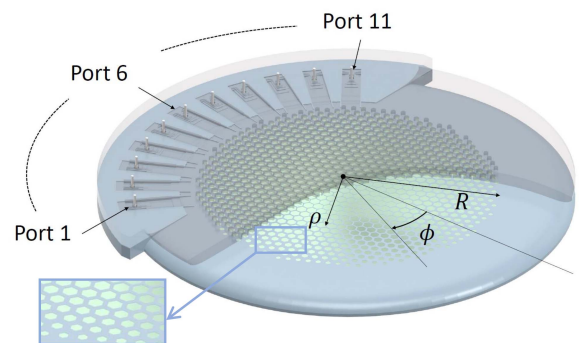


**FIGURE 12.** Exploded view of the proposed lens antenna. The zoom-in figure on the left illustrates the gradual change in the unit cell distribution of the lens. The PCBs are placed in a metallic casing that is terminated in a flare.

A detailed view of the proposed Luneburg lens antenna implemented with the structure analyzed in Fig. 11 is presented in Fig. 12. The Luneburg lens has a radius of  $R = 50$  mm and is fed by 11 rectangular waveguides, evenly distributed from  $-50^\circ$  to  $50^\circ$ . The metallic casing is terminated in a flare to match the impedance of the PPW to the free-space impedance. The design of the flare and feeding waveguides is detailed in [53].



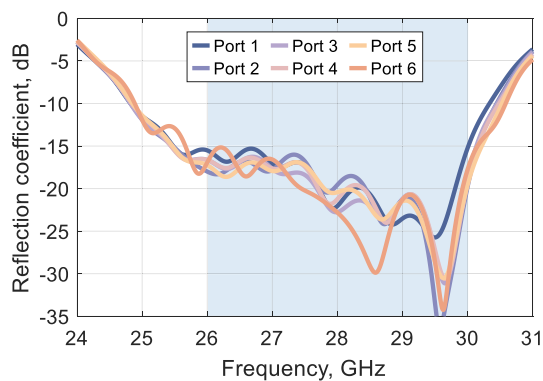


**FIGURE 13.** Simulated reflection coefficient of the Luneburg lens antenna shown in Fig. 12. Port numbers are indicated in Fig. 12.

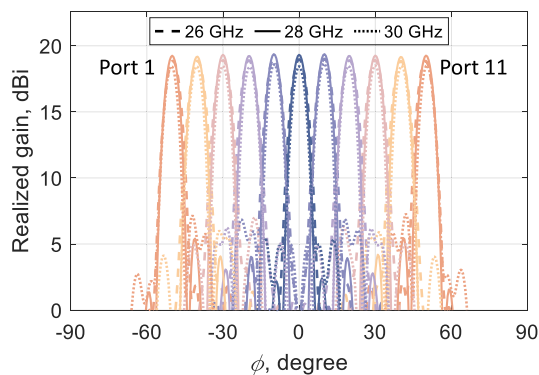


**FIGURE 15.** Simulated *H*-plane realized gain patterns at 26, 28, and 30 GHz. Port numbers are indicated in Fig. 12.

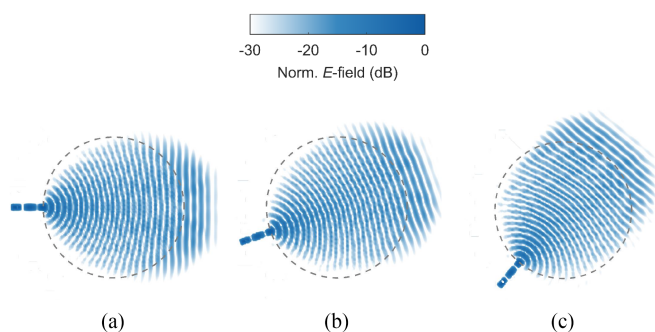


**FIGURE 14.** Simulated (CST Microwave Studio) normalized distribution of the electric field amplitude in the lens antenna at 27 GHz when excited from (a) 0°, (b) 20°, and (c) 50°.

The performance of the antenna is then analyzed with a full-wave simulation using CST Microwave Studio. The calculated reflection coefficients are plotted in Fig. 13, and are below  $-15$  dB from 26 to 30 GHz for all ports.

The normalized electric field distribution at 27 GHz when the antenna is fed from 0°, 20°, and 50° are presented in Fig. 14. The lens visibly transforms the cylindrical wave from the input into a quasi-planar wave on the opposite side over a wide scanning range.

Simulated *H*-plane realized gain patterns at 26, 28, and 30 GHz are shown in Fig. 15. Simulations clearly show that the antenna can produce a high-directive steerable beam that is stable with frequency.

### V. CONCLUSION

In this article, we provide a comprehensive theoretical analysis of the dispersion properties of metasurfaces with a hexagonal lattice, which offers higher design flexibilities and shows promising characteristics, such as excellent isotropy and wide bandwidth. Our study starts by briefly revisiting the relationship between the periodicity of the underlying geometry of a periodic structure and its dispersion properties. It allows us to analyze the hexagonal lattice periodic structure when its unit cell is taken as its primitive cell, as well as a rectangular supercell. This analysis, along with the study of

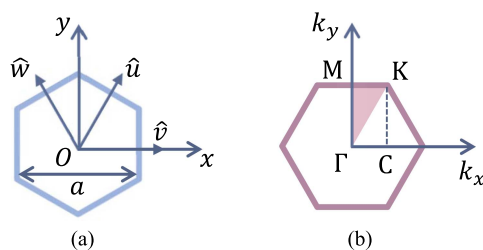


**FIGURE 16.** (a) WS primitive cell of a hexagonal periodic structure.  $\hat{w}$ ,  $\hat{u}$  and  $\hat{v}$  are perpendicular to the sides. (b) Brillouin zone of the hexagonal periodic structure. The irreducible Brillouin zone is assumed to be triangular and shaded pink.

the relations between the dispersion diagrams of both types of cells, brings great convenience when using the eigensolver tool of commercial software packages that cannot handle periodic conditions on non-orthogonal boundaries. Furthermore, we have explored the characteristics of hexagonal lattices with higher symmetries, including glide symmetry and mirrored half-turn symmetry. To illustrate the potential practical usefulness of the theoretical analysis, we present simulation results of hexagonal dielectric-filled holey periodic structures. In particular, we have designed and simulated a graded-index Luneburg lens antenna with a mirrored half-turn symmetric hexagonal lattice working in the  $K_a$ -band. The simulations clearly show that the antenna produces highly directive steerable beams that are stable over frequency. This approach to periodic structure analysis can be further applied to 3D periodic structures, allowing us to benefit from their properties in microwave engineering applications.

### APPENDIX A

In Appendix A, we detail the simulation settings for a 2D hexagonal periodic structure in the eigensolver tool of the electromagnetic simulation software ANSYS HFSS.

The primitive cell of a hexagonal periodic structure is as illustrated in Fig. 16(a). The length of its short diagonal is  $a$ .  $\hat{w}$ ,  $\hat{u}$ , and  $\hat{v}$  are three unit vectors perpendicular to the sides of the primitive unit cell, corresponding to three periodic directions.

These vectors are given by

$$\hat{\mathbf{u}} = \frac{1}{2}\hat{\mathbf{x}} + \frac{\sqrt{3}}{2}\hat{\mathbf{y}}, \quad \hat{\mathbf{w}} = -\frac{1}{2}\hat{\mathbf{x}} + \frac{\sqrt{3}}{2}\hat{\mathbf{y}}, \quad \hat{\mathbf{v}} = \hat{\mathbf{x}}. \quad (9)$$

In ANSYS HFSS, a pair of periodic ('Primary-Secondary') boundary conditions can be defined along each direction. To obtain the dispersion diagram following a certain path in the Brillouin zone, we need to know the corresponding phase shift along the  $\hat{\mathbf{w}}$ ,  $\hat{\mathbf{u}}$ , and  $\hat{\mathbf{v}}$  directions, so that the appropriate settings can be applied in the simulator. The phase associated with a wavevector  $\mathbf{k}$  along an arbitrary direction in the direct space defined by  $\mathbf{r}$  is calculated as

$$\phi_{\mathbf{r}}(\mathbf{r}) = \mathbf{k} \cdot \mathbf{r}\hat{\mathbf{r}}. \quad (10)$$

As our structure under study has a triangular irreducible Brillouin zone, shaded pink in Fig. 16(b), the settings to obtain the dispersion diagram following the path  $\Gamma$ -M-K- $\Gamma$  are detailed below.

- Path  $\Gamma \rightarrow \text{M}$ .

The points  $\Gamma$  and M in the reciprocal  $(k_x, k_y)$  space are given by

$$\Gamma = (0, 0), \quad \text{M} = \frac{2\pi}{a} \left( 0, \frac{1}{\sqrt{3}} \right) \quad (11)$$

which implies that the corresponding wavevector is

$$\mathbf{k}_{\text{M}} = \frac{2\pi}{a} \frac{1}{\sqrt{3}} \hat{\mathbf{y}}. \quad (12)$$

The phase associated with this wavevector along the  $\hat{\mathbf{u}}$  direction (that is,  $\mathbf{r} = u\hat{\mathbf{u}}$ ) is obtained as

$$\phi_u(u) = \mathbf{k}_{\text{M}} \cdot u\hat{\mathbf{u}} = \frac{2\pi}{a} \frac{1}{\sqrt{3}} \hat{\mathbf{y}} \cdot u \left( \frac{1}{2}\hat{\mathbf{x}} + \frac{\sqrt{3}}{2}\hat{\mathbf{y}} \right) = \pi \frac{u}{a}. \quad (13)$$

Within the unit cell, the distance along the  $\mathbf{u}$  direction between its boundaries is  $a$ . This means that the phase along this direction varies from  $\phi_u(0) = 0$  to  $\phi_u(a)$ ; that is, the range of variation of the phase shift is

$$0 \leq \Delta\phi_u \leq \pi. \quad (14)$$

A similar procedure can be followed to find phase shifts within the unit cell along the directions  $\mathbf{u}$  and  $\mathbf{v}$ , resulting in

$$0 \leq \Delta\phi_w \leq \pi \quad (15)$$

$$\Delta\phi_v = 0. \quad (16)$$

- Path M  $\rightarrow$  K.

The phase along the path M  $\rightarrow$  K can be expressed as

$$\phi^{\text{M} \rightarrow \text{K}} = \phi^{\Gamma \rightarrow \text{M}} + \Delta\phi^{\Gamma \rightarrow \text{C}} \quad (17)$$

where  $\phi^{\Gamma \rightarrow \text{M}}$  is already known from the previous step. Therefore, the analysis of the path M  $\rightarrow$  K can be simplified to analyze the conditions of the path  $\Gamma \rightarrow \text{C}$ . The point C is given in the reciprocal space as  $(2\pi/3a, 0)$ ,

**TABLE 1.** Phase Shift Conditions for Propagation Along the Edges of the Irreducible Brillouin Zone

	$\Delta\phi_u$	$\Delta\phi_v$	$\Delta\phi_w$
$\Gamma \rightarrow \text{M}$	$[0, \pi]$	$[0, 0]$	$[0, \pi]$
$\text{M} \rightarrow \text{K}$	$[\pi, \pi + \pi/3]$	$[0, 0 + 2\pi/3]$	$[\pi, \pi - \pi/3]$
$\text{K} \rightarrow \Gamma$	$[4\pi/3, 0]$	$[2\pi/3, 0]$	$[2\pi/3, 0]$

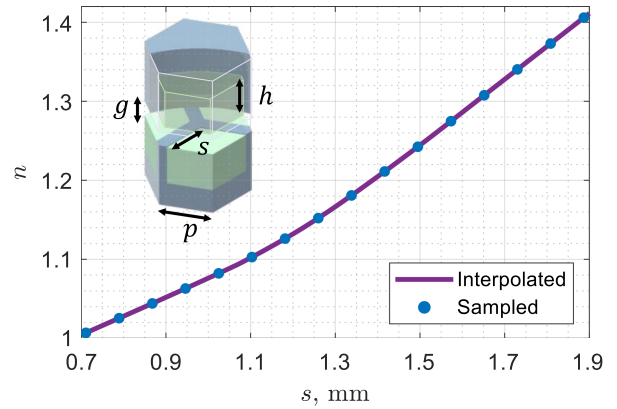


**FIGURE 17.** Effective refractive index ( $n$ ) versus sidelength of the hole ( $s$ ) before and after interpolation at 28 GHz. Structural parameters:  $p = 2$  mm,  $h = 1.575$  mm,  $g = 0.6$  mm, and the relative permittivity of the substrate  $\epsilon_r = 2.7$ .

thus we have

$$\mathbf{k}_{\text{C}} = \frac{2\pi}{a} \frac{1}{3} \hat{\mathbf{x}}. \quad (18)$$

The phase along the  $\hat{\mathbf{v}}$  direction (that is,  $\mathbf{r} = v\hat{\mathbf{v}}$ ) is given as

$$\phi_v(v) = \mathbf{k}_{\text{C}} \cdot v\hat{\mathbf{v}} = \frac{2\pi}{a} \frac{1}{3} \hat{\mathbf{x}} \cdot v\hat{\mathbf{x}} = \frac{2\pi}{3} \frac{v}{a} \quad (19)$$

which implies that the phase shift within the unit cell along the  $\hat{\mathbf{v}}$  direction is

$$0 \leq \Delta\phi_v \leq \frac{2\pi}{3}. \quad (20)$$

As the phase along the  $\hat{\mathbf{u}}$  direction is given by

$$\phi_u(u) = \mathbf{k}_{\text{C}} \cdot u\hat{\mathbf{u}} = \frac{2\pi}{a} \frac{1}{3} \hat{\mathbf{x}} \cdot u \left( \frac{1}{2}\hat{\mathbf{x}} + \frac{\sqrt{3}}{2}\hat{\mathbf{y}} \right) = \frac{\pi}{3} \frac{u}{a} \quad (21)$$

the phase shift within the unit cell along the  $\hat{\mathbf{v}}$  direction is

$$0 \leq \Delta\phi_u \leq \frac{\pi}{3}. \quad (22)$$

A similar procedure can be followed to find the following phase shift within the unit cell along the  $\mathbf{w}$  direction:

$$-\frac{\pi}{3} \leq \Delta\phi_w \leq 0. \quad (23)$$

- Path K  $\rightarrow$   $\Gamma$ .

In this case, we only have to recover the conditions to return to the origin, taking into account that

$$\phi^{\text{K} \rightarrow \Gamma} = -\phi^{\Gamma \rightarrow \text{K}}. \quad (24)$$

To summarize the range of variations in phase shifts, the phase conditions along the irreducible triangular Brillouin zone are listed in Table 1.

**APPENDIX B**

The lens design process can be broken down into the following three steps:

- ANSYS HFSS is used to simulate the unit cell and find how the effective refractive index ( $n$ ) of the unit cell varies with respect to the side length ( $s$ ) of the hole.
- The simulated sampled data are interpolated in MATLAB and used as a look-up table for the lens design. These data are also plotted in Fig. 17.
- The required refractive index of each unit cell is calculated based on its normalized centering position using the equation  $n(r) = \sqrt{2 - r^2}$ . Then, the corresponding hole size ( $s$ ) is searched in the look-up table on the basis of the calculated refractive index.

**REFERENCES**

[1] F. Alsolamy and A. Grbic, "Modal network formulation for the analysis and design of mode-converting metasurfaces in cylindrical waveguides," *IEEE Trans. Antennas Propag.*, vol. 69, no. 8, pp. 4598–4611, Aug. 2021.

[2] A. Monti, A. Alú, A. Toscano, and F. Bilotti, "Design of high-Q passband filters implemented through multipolar all-dielectric metasurfaces," *IEEE Trans. Antennas Propag.*, vol. 69, no. 8, pp. 5142–5147, Aug. 2021.

[3] Z. Wang, S. Zhao, and Y. Dong, "Pattern reconfigurable, low-profile, vertically polarized, ZOR-metasurface antenna for 5G application," *IEEE Trans. Antennas Propag.*, vol. 70, no. 8, pp. 6581–6591, Aug. 2022.

[4] O. Zetterstrom, R. Hamarneh, and O. Quevedo-Teruel, "Experimental validation of a metasurface luneburg lens antenna implemented with glide-symmetric substrate-integrated holes," *IEEE Antennas Wireless Propag. Lett.*, vol. 20, no. 5, pp. 698–702, May 2021.

[5] O. Quevedo-Teruel et al., "Roadmap on metasurfaces," *J. Opt.*, vol. 21, 2019, Art. no. 073002.

[6] N. W. Ashcroft and N. S. D. Mermin, *Solid State Physics*. Eastbourne, U.K.: Holt- Saunders, 1976.

[7] J. D. Joannopoulos, S. G. Johnson, J. N. Winn, and R. D. Meade, *Photonic Crystals*, 2nd ed. Princeton, NJ, USA: Princeton Univ. Press, 2007.

[8] L. Brillouin, *Wave Propagation in Periodic Structures: Electric Filters and Crystal Lattices*. New York, NY, USA: McGraw-Hill, 1946.

[9] S. Enoch, G. Tayeb, and B. Gralak, "The richness of the dispersion relation of electromagnetic bandgap materials," *IEEE Trans. Antennas Propag.*, vol. 51, no. 10, pp. 2659–2666, Oct. 2003.

[10] Q. Chen, F. Mesa, X. Yin, and O. Quevedo-Teruel, "Accurate characterization and design guidelines of glide-symmetric holey EBG," *IEEE Trans. Microw. Theory Techn.*, vol. 68, pp. 4984–4994, Dec. 2020.

[11] Q. Zeng, Z. Xue, W. Ren, and W. Li, "Dual-band beam-scanning antenna using rotatable planar phase gradient transmitarrays," *IEEE Trans. Antennas Propag.*, vol. 68, no. 6, pp. 5021–5026, Jun. 2020.

[12] L.-X. Wu, K. Chen, T. Jiang, J. Zhao, and Y. Feng, "Circular-polarization-selective metasurface and its applications to transmit-reflect-array antenna and bidirectional antenna," *IEEE Trans. Antennas Propag.*, vol. 70, no. 11, pp. 10207–10217, Nov. 2022.

[13] M. Saikia, K. V. Srivastava, and S. A. Ramakrishna, "Frequency-shifted reflection of electromagnetic waves using a time-modulated active tunable frequency-selective surface," *IEEE Trans. Antennas Propag.*, vol. 68, no. 4, pp. 2937–2944, Apr. 2020.

[14] S. Sengupta, D. R. Jackson, A. T. Almutawa, H. Kazemi, F. Capolino, and S. A. Long, "A cross-shaped 2-D periodic leaky-wave antenna," *IEEE Trans. Antennas Propag.*, vol. 68, no. 3, pp. 1289–1301, Mar. 2020.

[15] P. J. Crepeau and P. R. McIsaac, "Consequences of symmetry in periodic structures," *Proc. IEEE*, vol. 52, no. 1, pp. 33–43, Jan. 1964.

[16] A. Hessel, M. H. Chen, R. C. M. Li, and A. A. Oliner, "Propagation in periodically loaded waveguides with higher symmetries," *Proc. IEEE*, vol. 61, no. 2, pp. 183–195, Feb. 1973.

[17] P. Castillo-Tapia, K. Van Gassen, Q. Chen, F. Mesa, Z. Sipus, and O. Quevedo-Teruel, "Dispersion analysis of twist-symmetric dielectric waveguides," *Photonics*, vol. 8, no. 6, 2021, Art. no. 206.

[18] J.-M. Poyanco, O. Zetterstrom, P. Castillo-Tapia, N. J. G. Fonseca, F. Pizarro, and O. Quevedo-Teruel, "Two-dimensional glide-symmetric dielectric structures for planar graded-index lens antennas," *IEEE Antennas Wireless Propag. Lett.*, vol. 20, no. 11, pp. 2171–2175, Nov. 2021.

[19] Q. Chen, F. Mesa, P. Padilla, X. Yin, and O. Quevedo-Teruel, "Efficient leaky-lens antenna at 60 GHz based on a substrate-integrated-hole metasurface," *IEEE Trans. Antennas Propag.*, vol. 68, no. 12, pp. 7777–7784, Dec. 2020.

[20] G. Valerio, F. Ghasemifard, Z. Sipus, and O. Quevedo-Teruel, "Glide-symmetric all-metal holey metasurfaces for low-dispersive artificial materials: Modeling and properties," *IEEE Trans. Microw. Theory Techn.*, vol. 66, no. 7, pp. 3210–3223, Jul. 2018.

[21] F. Mesa, G. Valerio, R. Rodríguez-Berral, and O. Quevedo-Teruel, "Simulation-assisted efficient computation of the dispersion diagram of periodic structures," *IEEE Antennas Propag. Mag.*, vol. 63, no. 5, pp. 33–45, Oct. 2021.

[22] M. Bagheriasl, O. Quevedo-Teruel, and G. Valerio, "Bloch analysis of artificial lines and surfaces exhibiting glide symmetry," *IEEE Trans. Microw. Theory Techn.*, vol. 67, no. 7, pp. 2618–2628, Jul. 2019.

[23] S. J. Skirvin, V. Fedun, and G. Verth, "I. The effect of symmetric and spatially varying equilibria and flow on MHD wave modes: Slab geometry," *Monthly Notices Roy. Astronomical Soc.*, vol. 504, no. 3, pp. 4077–4092, 2021.

[24] M. Fazelpour, P. Shankar, and J. D. Summers, "A unit cell design guideline development method for meso-scaled periodic cellular material structures," *J. Eng. Mater. Technol.*, vol. 141, no. 4, 2019, Art. no. 041004.

[25] S. M. Gilbert et al., "Alternative stacking sequences in hexagonal boron nitride," *2D Mater.*, vol. 6, no. 2, 2019, Art. no. 021006.

[26] J. I. Wang et al., "Hexagonal boron nitride as a low-loss dielectric for superconducting quantum circuits and qubits," *Nature Mater.*, vol. 21, no. 4, pp. 398–403, 2022.

[27] K. C. Chen, J. W. Yang, Y.-C. Yang, C. F. Khin, and M. N. M. Kehn, "Plasmonic Luneburg lens antenna synthesized by metasurfaces with hexagonal lattices," *Opt. Exp.*, vol. 25, no. 22, pp. 27405–27414, 2017.

[28] J. P. Pereira, J. P. da Silva, and H. D. de Andrade, "A new design and analysis of a hexagonal PBG microstrip antenna," *Microw. Opt. Technol. Lett.*, vol. 57, no. 9, pp. 2147–2151, 2015.

[29] M. Yoo and S. Lim, "Polarization-independent and ultrawideband metamaterial absorber using a hexagonal artificial impedance surface and a resistor-capacitor layer," *IEEE Trans. Antennas Propag.*, vol. 62, no. 5, pp. 2652–2658, May 2014.

[30] H. Jiang et al., "Transparent and ultra-wideband metamaterial absorber using coupled hexagonal combined elements," *Opt. Exp.*, vol. 29, no. 18, pp. 29439–29448, 2021.

[31] Y. Kim and J.-H. Lee, "Design of broadband and wide-angle hexagonal metamaterial absorber based on optimal tiling of rhombus carbon pixels and implantation of copper cylinders," *Symmetry*, vol. 13, no. 11, 2021, Art. no. 2045.

[32] S. Yang, O. Zetterstrom, Z. Xue, F. Mesa, and O. Quevedo-Teruel, "Hexagonal higher-symmetric dielectric periodic structures for planar graded-index lenses," *Appl. Phys. Lett.*, vol. 123, p. 011707(1-5), 2023.

[33] A. H. C. Neto, F. Guinea, N. M. Peres, K. S. Novoselov, and A. K. Geim, "The electronic properties of graphene," *Rev. Modern Phys.*, vol. 81, pp. 109–162, 2009.

[34] S. Haykin, *Communication Systems*, 5th ed. Hoboken, NJ, USA: Wiley, 2009.

[35] S. Bittner, B. Dietz, M. Miski-Oglu, P. O. Iriarte, A. Richter, and F. Schäfer, "Observation of a dirac point in microwave experiments with a photonic crystal modeling graphene," *Phys. Rev. B*, vol. 82, 2010, Art. no. 014301.

[36] K. S. Novoselov, "Nobel lecture: Graphene: Materials in the flatland," *Rev. Mod. Phys.*, vol. 83, pp. 837–849, 2011.

[37] G. Berkolaiko and A. Comech, "Symmetry and dirac points in graphene spectrum," *J. Spectral Theory*, vol. 8, pp. 1099–1147, 2018.

- [38] S. R. Zandbergen and M. J. D. Dood, "Experimental observation of strong edge effects on the pseudodiffusive transport of light in photonic graphene," *Phys. Rev. Lett.*, vol. 104, 2010, Art. no. 043903.
- [39] U. Kuhl et al., "Dirac point and edge states in a microwave realization of tight-binding graphene-like structures," *Phys. Rev. B*, vol. 82, 2010, Art. no. 094308.
- [40] R. Mittra and S. Laxpati, "Propagation in a wave guide with glide reflection symmetry," *Can. J. Phys.*, vol. 43, no. 2, pp. 353–372, 1965.
- [41] R. Kieburz and J. Impagliazzo, "Multimode propagation on radiating traveling-wave structures with glide-symmetric excitation," *IEEE Trans. Antennas Propag.*, vol. 18, no. 1, pp. 3–7, Jan. 1970.
- [42] O. Quevedo Teruel, Q. Chen, F. Mesa, N. J. G. Fonseca, and G. Valerio, "On the benefits of glide symmetries for microwave devices," *IEEE J. Microwaves*, vol. 1, no. 1, pp. 457–469, Jan. 2021.
- [43] M. Ebrahimpouri, E. Rajo-Iglesias, Z. Sipus, and O. Quevedo-Teruel, "Cost-effective gap waveguide technology based on glide-symmetric holey EBG structures," *IEEE Trans. Microw. Theory Techn.*, vol. 66, no. 2, pp. 927–934, Feb. 2018.
- [44] A. Vosoogh, H. Zirath, and Z. S. He, "Novel air-filled waveguide transmission line based on multilayer thin metal plates," *IEEE Trans. THz Sci. Technol.*, vol. 9, no. 3, pp. 282–290, May 2019.
- [45] A. Monje-Real, N. J. G. Fonseca, O. Zetterstrom, E. Pucci, and O. Quevedo-Teruel, "Holey glide-symmetric filters for 5G at millimeter-wave frequencies," *IEEE Microw. Wireless Compon. Lett.*, vol. 30, no. 1, pp. 31–34, Jan. 2020.
- [46] A. Alex-Amor et al., "Glide-symmetric metallic structures with elliptical holes for lens compression," *IEEE Trans. Microw. Theory Techn.*, vol. 68, no. 10, pp. 4236–4248, Oct. 2020.
- [47] Q. Chen, F. Giusti, G. Valerio, F. Mesa, and O. Quevedo-Teruel, "Anisotropic glide-symmetric substrate-integrated-hole metasurface for a compressed ultrawideband luneburg lens," *Appl. Phys. Lett.*, vol. 118, no. 8, 2021, Art. no. 084102.
- [48] C. Pfeiffer and A. Grbic, "A printed, broadband Luneburg lens antenna," *IEEE Trans. Antennas Propag.*, vol. 58, no. 9, pp. 3055–3059, Sep. 2010.
- [49] M. Liang, W.-R. Ng, K. Chang, K. Gbele, M. E. Gehm, and H. Xin, "A 3-D Luneburg lens antenna fabricated by polymer jetting rapid prototyping," *IEEE Trans. Antennas Propag.*, vol. 62, no. 4, pp. 1799–1807, Apr. 2014.
- [50] Y. J. Cheng et al., "Substrate integrated waveguide (SIW) Rotman lens and its Ka-band multibeam array antenna applications," *IEEE Trans. Antennas Propag.*, vol. 56, no. 8, pp. 2504–2513, Aug. 2008.
- [51] R. Hansen, "Design trades for Rotman lenses," *IEEE Trans. Antennas Propag.*, vol. 39, no. 4, pp. 464–472, Apr. 1991.
- [52] O. Quevedo-Teruel, J. Miao, M. Mattsson, A. Algaba-Brazalez, M. Johansson, and L. Manholm, "Glide-symmetric fully metallic luneburg lens for 5G communications at Ka-band," *IEEE Antennas Wireless Propag. Lett.*, vol. 17, no. 9, pp. 1588–1592, Sep. 2018.
- [53] R. Hamarneh, O. Zetterstrom, and O. Quevedo-Teruel, "Glide-symmetric Luneburg lens using substrate-integrated-holes for 5G communications at Ka-band," in *Proc. IEEE 14th Eur. Conf. Antennas Propag.*, 2020, pp. 1–5.